DTU Library

Time-dependent density-functional theory in the projector augmented-wave method

Walter, Michael; Häkkinen, Hannu; Lehtovaara, Lauri; Puska, Martti; Enkovaara, Jussi; Rostgaard, Carsten; Mortensen, Jens Jørgen

Link back to DTU Orbit

Time-dependent density-functional theory in the projector augmented-wave method

Michael Walter,[1,a)] Hannu Häkkinen,[1,2] Lauri Lehtovaara,[3] Martti Puska,[3] Jussi Enkovaara,[4] Carsten Rostgaard,[5] and Jens Jørgen Mortensen[5]

[1]*Department of Physics, Nanoscience Center, University of Jyväskylä, FIN-40014 Jyväskylä, Finland*
[2]*Department of Chemistry, Nanoscience Center, University of Jyväskylä, FIN-40014, Jyväskylä, Finland*
[3]*Department of Engineering Physics, Helsinki University of Technology, P.O. Box 1100,*
FIN-02015 TKK, Finland
[4]*CSC Scientific Computing Ltd., FI-02101 Espoo, Finland*
[5]*CAMd, Department of Physics, Technical University of Denmark, DK-2800 Lyngby, Denmark*

We present the implementation of the time-dependent density-functional theory both in linear-response and in time-propagation formalisms using the projector augmented-wave method in real-space grids. The two technically very different methods are compared in the linear-response regime where we found perfect agreement in the calculated photoabsorption spectra. We discuss the strengths and weaknesses of the two methods as well as their convergence properties. We demonstrate different applications of the methods by calculating excitation energies and excited state Born–Oppenheimer potential surfaces for a set of atoms and molecules with the linear-response method and by calculating nonlinear emission spectra using the time-propagation method. © 2008 American Institute of Physics. [DOI: 10.1063/1.2943138]

I. INTRODUCTION

The density-functional theory[1,2] (DFT) has been very successful for ground-state calculations of molecular and condensed-matter systems due to its favorable balance of cost against accuracy. Properties such as ground-state total energies, lattice constants, and equilibrium geometries are nowadays calculated routinely for systems containing up to a few hundred atoms. However, there are several scientifically and technologically interesting quantities which are related to excited states of the system and are thus beyond the realm of the standard DFT. In recent years, the time-dependent DFT (TDDFT) (Ref. 3) has become a popular tool for calculating excited-state properties such as linear and nonlinear optical responses.[4–9]

The most general realization of the TDDFT is the time-propagation scheme[5] in which the time-dependent Kohn–Sham (KS) equations are integrated over the time domain. In the linear-response regime the excitation energies can also be calculated in the frequency space by solving a matrix equation in a particle-hole basis.[4] This is the so-called linear-response scheme. The time-propagation and the linear-response scheme are complementary as they have different advantages and disadvantages. For example, the linear-response scheme provides all the excitations in a single calculation, while the time-propagation provides only the excitations corresponding to the given initial perturbation and several separate calculations may be needed. On the other hand, the time-propagation has a wider applicability as also non-linear-response phenomena, such as the high-harmonics generation in intense laser beams and general time-

dependent phenomena, in which for example the ionic structure relaxes as a function of time, can be studied. Computationally, the time-propagation scales more favorably with the system size than the linear-response scheme. However, the prefactor in time-propagation is larger, so that the cross-over in efficiency is reached at relatively large systems.

Previously, there have been several implementations of the linear-response and the time-propagation formalisms using a variety of methods such as localized basis sets,[10,11] plane waves,[12–15] and real-space grids.[5,16,17] The plane-wave and the real-space implementations have used the pseudopotential approximation which has been either of the norm-conserving or ultrasoft flavor. To our knowledge, the projector augmented-wave (PAW) method[18] has not been used in time-dependent density-functional calculations previously. Here, we present implementation of both time-propagation and linear-response TDDFT in the electronic-structure program GPAW,[19,20] which uses the PAW method and uniform real-space grids.

The real-space PAW method has several advantages both in ground-state and in time-dependent calculations. First, there is a single convergence parameter, the grid spacing, which controls the accuracy of the discretization. Different boundary conditions can be handled easily and especially the ability to treat finite systems without supercells is important for TDDFT. The PAW method can be applied on the same footing to all elements, for example, it provides a reliable description of the transition metal elements and the first row elements with open p-shells. These are often problematic for standard pseudopotentials. Also, the PAW method reduces the number of grid points required for accurate calculations in comparison with pseudopotential calculations. Thus, the dimension of the Hamiltonian matrix is reduced and one is

a)Electronic mail: michael.walter@phys.jyu.fi.

also allowed to use longer time steps in time-propagation.[15] Finally, the real-space formalism allows efficient parallelization with domain-decomposition techniques.

The present paper is organized as follows. In Sec. II A we present the basic features of the PAW method. The linear-response formulation of the TDDFT within the PAW method is presented in Sec. II B and the time-propagation scheme is reviewed in Sec. II C. In Sec. III we show that the two methods give identical results in the linear-response regime by calculating the optical absorption spectra for the Na_2 and C_6H_6 molecules. Next, we focus on the linear-response scheme and calculate excitation energies for a set of divalent atoms followed by Born–Oppenheimer potentials of excited states of Na_2. The applicability of the time-propagation in the nonlinear regime is demonstrated by calculating emission spectra of the Be atom in strong laser fields. The convergence properties of the two methods are discussed in Sec. IV. Finally, we give a brief summary in Sec. V.

II. THEORY

A. Ground state

The implementation of the PAW method using a real-space grid is explained in detail in Ref. 19. We will give here just a short introduction with the main purpose of defining the quantities needed for the time-propagation and linear-response calculation. In the PAW method, a true all-electron KS wave function ψ_n can be obtained through a linear transformation from a smooth pseudo-wave-function $\tilde{\psi}_n$ via

$$\psi_n(\mathbf{r}) = \hat{\mathcal{T}}\tilde{\psi}_n, \tag{1}$$

where n denotes a combined band and spin index. Using the explicit representation of $\hat{\mathcal{T}}$, the KS wave functions can be expressed as

$$\psi_n(\mathbf{r}) = \tilde{\psi}_n(\mathbf{r}) + \sum_a (\psi_n^a(\mathbf{r} - \mathbf{R}_a) - \tilde{\psi}_n^a(\mathbf{r} - \mathbf{R}_a)), \tag{2}$$

where ψ_n^a and $\tilde{\psi}_n^a$ are the all-electron and smooth continuations of ψ_n inside the augmentation region of the atom a at position $\mathbf{R}_a$, respectively. Their difference vanishes by definition outside the augmentation region. ψ_n^a and $\tilde{\psi}_n^a$ may be expanded in terms of atom-centered all-electron wave functions ϕ^a and their smooth counterparts $\tilde{\phi}^a$, respectively, i.e.,

$$\psi_n^a(\mathbf{r}) = \sum_j P_{nj}^a \phi_j^a(\mathbf{r}), \quad \tilde{\psi}_n^a(\mathbf{r}) = \sum_j P_{nj}^a \tilde{\phi}_j^a(\mathbf{r}), \tag{3}$$

with the same coefficients $P_{nj}^a = \langle p_j | \psi_n \rangle$, where the p_j are the so called projector functions.[18,19] The main quantity of DFT, the electron density $n(\mathbf{r})$ has a similar partitioning as the wave functions (this behavior can be shown to be true for all quantities that can be expressed as expectation values of local operators[18]). Thus,

$$n(\mathbf{r}) = \tilde{n}(\mathbf{r}) + \sum_a (n^a(\mathbf{r} - \mathbf{R}_a) - \tilde{n}^a(\mathbf{r} - \mathbf{R}_a)), \tag{4}$$

where the all-electron density inside the augmentation region

$$n^a(\mathbf{r}) = \sum_{i_1 i_2} D_{i_1 i_2}^a \phi_{i_1}^a(\mathbf{r}) \phi_{i_2}^a(\mathbf{r}) \tag{5}$$

and its smooth counterpart

$$\tilde{n}^a(\mathbf{r}) = \sum_{i_1 i_2} D_{i_1 i_2}^a \tilde{\phi}_{i_1}^a(\mathbf{r}) \tilde{\phi}_{i_2}^a(\mathbf{r}) \tag{6}$$

appear. Denoting the ground-state occupation numbers by f_n, the above atomic density matrix can be expressed as[19]

$$D_{i_1 i_2}^a = \sum_n P_{n i_1}^{a*} f_n P_{n i_2}^a. \tag{7}$$

B. Linear response

In the following we discuss the linear-response theory in the TDDFT from a practical view, rather than from its formal derivation which can be found in the original references[4,10,21] or in more recent work.[22] We follow closely the notation used by Casida,[4] who showed that in the linear-response TD-DFT the calculation of excitation energies can be reduced to solving the eigenvalue equation of the following form:

$$\Omega F_I = \omega_I^2 F_I, \tag{8}$$

where $\hbar\omega_I$ is the transition energy from the ground state to the excited state I. Expanding the matrix $\boldsymbol{\Omega}$ in KS single particle-hole excitations leads to

$$\Omega_{ij\sigma,kq\tau} = \delta_{ik}\delta_{jq}\delta_{\sigma\tau}\varepsilon_{ij\sigma}^2 + 2\sqrt{f_{ij\sigma}\varepsilon_{ij\sigma}f_{kq\tau}\varepsilon_{kq\tau}}K_{ij\sigma,kq\tau}, \tag{9}$$

where $\varepsilon_{ij\sigma} = \varepsilon_{j\sigma} - \varepsilon_{i\sigma}$ are the energy differences and $f_{ij\sigma} = f_{i\sigma} - f_{j\sigma}$ are the occupation number differences of the KS states. The indices i, j, k, and q are band indices, whereas σ and τ denote spin projection indices. The coupling matrix can be split into two parts $K_{ij\sigma,kq\tau} = K_{ij\sigma,kq\tau}^{\text{RPA}} + K_{ij\sigma,kq\tau}^{\text{xc}}$. The former is the so-called random phase approximation (RPA) part,

$$K_{ij\sigma,kq\tau}^{\text{RPA}} = \int d\mathbf{r}_1 d\mathbf{r}_2 \frac{n_{ij\sigma}^*(\mathbf{r}_1) n_{kq\tau}(\mathbf{r}_2)}{|\mathbf{r}_1 - \mathbf{r}_2|} =: (n_{ij\sigma}|n_{kq\tau}), \tag{10}$$

where $n_{ij\sigma}$ is the i,j density matrix element or pair density corresponding to the spin σ. $K_{ij\sigma,kq\tau}^{\text{RPA}}$ describes the effect of the linear density response via the classical Hartree energy. The second is the exchange-correlation part,

$$K_{ij\sigma,kq\tau}^{\text{xc}} = \int d\mathbf{r}_1 d\mathbf{r}_2 n_{ij\sigma}^*(\mathbf{r}_1) \frac{\delta^2 E_{\text{xc}}}{\delta\rho_\sigma(\mathbf{r}_1)\delta\rho_\tau(\mathbf{r}_2)} n_{kq\tau}(\mathbf{r}_2), \tag{11}$$

where ρ_σ is the spin density. $K_{ij\sigma,kq\tau}^{\text{xc}}$ describes the effect of the linear density response via the exchange and correlation energy.

We discuss the forms of the coupling matrix for the two parts separately and suppress the explicit dependence on the spin projection unless it is explicitly needed. In both parts of the coupling matrix the pair density $n_{ij}(\mathbf{r}) = \psi_i^*(\mathbf{r})\psi_j(\mathbf{r})$ appears. This quantity can be partitioned in the same way as the electron density, i.e.,

$$n_{ij} = \tilde{n}_{ij} + \sum_a (n_{ij}^a - \tilde{n}_{ij}^a), \tag{12}$$

where we have dropped the dependence on the position for brevity. Inserting this expression directly into the integral in

Eq. (10) would lead to overlaps of different augmentation spheres due to the nonlocality of the Coulomb operator $|\mathbf{r}_1 - \mathbf{r}_2|^{-1}$. These overlaps have to be avoided. The same problem appears already in the calculations of the Hartree energy in the ground-state problem.[18,19] It can be solved by introducing compensation charge densities $\widetilde{Z}_{ij}^a$, defined to fulfill

$$\int d\mathbf{r}_2 \frac{n_{ij}^a(\mathbf{r}_2) - \widetilde{n}_{ij}^a(\mathbf{r}_2) - \widetilde{Z}_{ij}^a(\mathbf{r}_2)}{|\mathbf{r}_1 - \mathbf{r}_2|} = 0, \tag{13}$$

for $|\mathbf{r}_1 - \mathbf{R}_a| > r_c^a$, i.e., outside the augmentation sphere. The compensation charge densities can be expanded in terms of spherical harmonics Y_L,[18,19]

$$\widetilde{Z}_{ij}^a(\mathbf{r}) = \sum_L Q_{L,ij}^a g_l^a(r) Y_L(\hat{\mathbf{r}}), \tag{14}$$

where L stands for the combined values of angular momentum quantum numbers l and m. The choice of local functions $g_l^a(r)$ is arbitrary as long as they fulfill

$$\int dr\, r^{l+2} g_l^a(r) = 1, \tag{15}$$

and they are sufficiently localized inside the augmentation sphere. For the particular choice of $g_l^a(r)$ in our calculations

we refer to Eq. (B1) in Ref. 19. Due to Eq. (13) the coefficients $Q_{L,ij}^a$ have to be

$$Q_{L,ij} = \sum_{i_1 i_2} \Delta_{L,i_1 i_2} P_{i i_1}^a P_{j i_2}^a, \tag{16}$$

with the constants

$$\Delta_{L,i_1 i_2} = \int d\mathbf{r}\, r^l Y_L(\hat{\mathbf{r}}) [\phi_{i_1}^a(\mathbf{r}) \phi_{i_2}^a(\mathbf{r}) - \widetilde{\phi}_{i_1}^a(\mathbf{r}) \widetilde{\phi}_{i_2}^a(\mathbf{r})]. \tag{17}$$

Using the shorthand

$$\widetilde{\rho}_{ij}(\mathbf{r}) := \widetilde{n}_{ij}(\mathbf{r}) + \sum_a \widetilde{Z}_{ij}^a(\mathbf{r} - \mathbf{R}_a), \tag{18}$$

we may write the RPA part of the kernel in the following form:

$$K_{ij,kq}^{\mathrm{RPA}} = (\widetilde{\rho}_{ij} | \widetilde{\rho}_{kq}) + \sum_a \Delta K_{ij,kq}^{\mathrm{RPA},a}, \tag{19}$$

which has the desired partitioning in a pure smooth part $(\widetilde{\rho}_{ij} | \widetilde{\rho}_{kq})$ and local corrections $\Delta K_{ij\sigma,kq\tau}^{\mathrm{RPA},a}$ inside the augmentation spheres. The explicit form of these corrections is given in Appendix A [Eq. (A3)].

The exchange-correlation part of the coupling matrix is evaluated in a finite-difference scheme[23,24] as

$$K_{ij\sigma,kq\tau}^{\mathrm{xc}}[n_\sigma, n_\tau] = \lim_{\varepsilon \to 0} \int d\mathbf{r}\, n_{ij\sigma}^*(\mathbf{r}) \frac{v_{\mathrm{xc}}^\sigma[n_\sigma, n_\tau + \varepsilon n_{kq\tau}](\mathbf{r}) - v_{\mathrm{xc}}^\sigma[n_\sigma, n_\tau - \varepsilon n_{kq\tau}](\mathbf{r})}{2\varepsilon}, \tag{20}$$

where we denote that $K_{ij\sigma,kq\tau}^{\mathrm{xc}}$ is a functional of the spin densities explicitly. The finite-difference scheme is quite insensitive to the actual numerical value for ε as will be shown in Sec. III. For the local density approximation (LDA) and the generalized gradient approximation for the electron exchange and correlation we can write

$$K_{ij\sigma,kq\tau}^{\mathrm{xc}}[n_\sigma, n_\tau] = \widetilde{K}_{ij\sigma,kq\tau}^{\mathrm{xc}}[\widetilde{n}_\sigma, \widetilde{n}_\tau] + \sum_a \Delta K_{ij\sigma,kq\tau}^{\mathrm{xc},a}, \tag{21}$$

where $\widetilde{K}_{ij\sigma,kq\tau}^{\mathrm{xc}}$ depends on the smooth densities and the corrections $\Delta K_{ij\sigma,kq\tau}^{\mathrm{xc},a}$ are localized inside the atomic augmentation spheres. The explicit form of these corrections is given in Appendix B [Eq. (B1)].

In optical absorption spectra not only the excitation energies but also the corresponding dipole oscillator strengths are of interest. They are dimensionless and can be written as

$$f_{I\alpha} = \frac{2m_e}{\hbar e^2} \omega_I \mu_{I\alpha}^2, \tag{22}$$

where m_e is the electron mass, e is the unit charge, and $\alpha = x, y, z$ denotes the direction of the light polarization. The dipole transition moment,

$$\boldsymbol{\mu}_I = -e \langle 0 | \sum_{k=1}^N \mathbf{r}_k | I \rangle, \tag{23}$$

is defined through the many-particle ground and excited states $|0\rangle$ and $|I\rangle$, respectively. Above, N is the number of electrons with their coordinates $\mathbf{r}_k$, $k = 1, \ldots, N$. In linear-response TDDFT the oscillator strength for a transition I can be obtained using the corresponding eigenvector F_I of the Ω matrix and the KS transition dipoles,

$$\boldsymbol{\mu}_{ij\sigma} = -e \langle \psi_{i\sigma} | \mathbf{r} | \psi_{j\sigma} \rangle, \tag{24}$$

between the KS states $\psi_{i\sigma}$ and $\psi_{j\sigma}$. The oscillator strengths are evaluated then as[4]

$$f_{I\alpha} = \frac{2m_e}{\hbar e^2} \left| \sum_{ij\sigma}^{f_{i\sigma} > f_{j\sigma}} (\boldsymbol{\mu}_{ij\sigma})_\alpha \sqrt{f_{ij\sigma} \varepsilon_{ij\sigma}} (F_I)_{ij\sigma} \right|^2. \tag{25}$$

In PAW the KS transition dipoles can be partitioned as

$$\boldsymbol{\mu}_{ij\sigma} = -e \langle \widetilde{\psi}_{i\sigma} | \mathbf{r} | \widetilde{\psi}_{j\sigma} \rangle + \sum_a \sum_{pq} P_{i\sigma p}^* P_{j\sigma q} \boldsymbol{\mu}_{pq}^a, \tag{26}$$

where the local corrections are

$$(\boldsymbol{\mu}_{pq}^a)_m = -e\sqrt{4\pi}\left[\frac{\Delta_{1m,pq}^a}{\sqrt{3}} + \Delta_{L=0,pq}^a(\mathbf{R}_a)_m\right], \qquad (27)$$

with the constants $\Delta_{L,pq}^a$ defined in Eq. (17).

C. Time-propagation

The scheme for propagating time-dependent KS wave functions within the ultrasoft pseudopotential or projector augmented-wave method was already described by Qian *et al.*[14] As our implementation follows closely theirs, it is reviewed only briefly here.

The all-electron time-dependent Schrödinger-type KS equation with the Hamiltonian $\hat{H}(t)$, i.e.,

$$i\hbar\frac{\partial}{\partial t}\psi_n(t) = \hat{H}(t)\psi_n(t), \qquad (28)$$

is transformed to the PAW formalism as follows. First the all-electron wave function is replaced by the projector operator operating on the pseudo-wave-function $\psi_n = \hat{T}\tilde{\psi}_n$. Then Eq. (28) is operated from the left by the adjoint operator $\hat{T}^\dagger$, i.e.,

$$i\hbar\hat{T}^\dagger\frac{\partial}{\partial t}\hat{T}\tilde{\psi}_n(t) = \hat{T}^\dagger\hat{H}(t)\hat{T}\tilde{\psi}_n(t). \qquad (29)$$

If the projector operator $\hat{T}$ is independent of time, i.e., the nuclei do not move, the above equation reads as

$$i\hbar\tilde{S}\frac{\partial}{\partial t}\tilde{\psi}_n(t) = \tilde{H}(t)\tilde{\psi}_n(t), \qquad (30)$$

where $\tilde{S} = \hat{T}^\dagger\hat{T}$ is the PAW overlap operator and $\tilde{H}(t) = \hat{T}^\dagger\hat{H}(t)\hat{T}$ is the time-dependent PAW Hamiltonian including the external time-dependent potential.

The linear absorption spectrum is obtained in the time-propagation scheme by applying a very weak delta-function pulse of a dipole field,[5]

$$\mathbf{E}(t) = \epsilon\mathbf{k^o}\delta(t)\frac{\hbar}{a_0 e}, \qquad (31)$$

to the system and then following the time-evolution of the dipole vector $\boldsymbol{\mu}(t)$. Above, ϵ is a unitless perturbation strength parameter, $\mathbf{k^o}$ is a unit vector giving the polarization direction of the field, and a_0 is the Bohr radius. The delta pulse excites all possible frequencies at time zero, so that the KS wave functions change instantaneously to

$$\psi(t=0^+) = \exp\left(i\frac{\epsilon}{a_0}\mathbf{k^o}\cdot\mathbf{r}\right)\psi(t=0^-). \qquad (32)$$

Then the system is let to evolve freely.

To see the connection to the linear-response calculations, we study the effect of the delta kick in the many-body picture. If the pulse strength is weak, i.e., $\epsilon \ll 1$, the time-dependent many-body wave function after the kick is

$$|\Psi(t=0^+)\rangle = \left(1 - i\frac{\epsilon}{ea_0}\mathbf{k^o}\cdot\hat{\boldsymbol{\mu}}\right)|0\rangle + O(\epsilon^2), \qquad (33)$$

where $\hat{\boldsymbol{\mu}} = -e\Sigma_{k=1}^N\mathbf{r}_k$ is the dipole operator. When the system evolves freely it can be expanded in eigenstates $|0\rangle$ and $|I\rangle$ of the unperturbed Hamiltonian as

$$|\Psi(t)\rangle = c_0|0\rangle + \sum_I e^{-i\omega_I t}c_I|I\rangle, \qquad (34)$$

with the coefficients

$$c_0 = 1 - i\frac{\epsilon}{ea_0}\mathbf{k^o}\cdot\langle 0|\hat{\boldsymbol{\mu}}|0\rangle, \qquad (35)$$

and

$$c_I = -i\frac{\epsilon}{ea_0}\mathbf{k^o}\cdot\langle I|\hat{\boldsymbol{\mu}}|0\rangle. \qquad (36)$$

The time-dependent density can be written as[25]

$$n(\mathbf{r},t) = n_0(\mathbf{r}) + \sum_I (e^{-i\omega_I t}c_I\langle 0|\hat{n}(\mathbf{r})|I\rangle + \text{c.c.}), \qquad (37)$$

where $\hat{n} = \Sigma_{k=1}^N\delta(\mathbf{r}-\mathbf{r}_k)$ denotes the density operator. In the absence of magnetic fields all states can be chosen to be real resulting in the time-dependent dipole moment $\boldsymbol{\mu}(t) = -e\int d\mathbf{r}\, n(\mathbf{r},t)\mathbf{r}$ of the following form:

$$\boldsymbol{\mu}(t) = \boldsymbol{\mu}(0) - \frac{2\epsilon}{ea_0}\sum_I \sin(\omega_I t)(\mathbf{k^o}\cdot\boldsymbol{\mu}_I)\boldsymbol{\mu}_I. \qquad (38)$$

From this the dipole transition moment and hence the oscillator strength can be extracted via the Fourier transform. In practice, one calculates the generalization of the oscillator strength, the dipole strength tensor with respect to the polarization direction, $\mathbf{k}^o$ via[14]

$$\mathbf{S}(\omega)\mathbf{k}^o = \frac{2m_e a_0}{e\hbar\pi}\omega\frac{1}{\epsilon}\int_0^T dt\,\sin(\omega t)g(t)[\boldsymbol{\mu}(0) - \boldsymbol{\mu}(t)], \qquad (39)$$

where T is the simulation time, and $g(t)$ is an envelope function being finite in the time window only. The envelope function, typically a Gaussian or an exponential decay, yields the shapes of the simulated spectral lines, Gaussians and Lorentzians, respectively, removing the effects of the finite simulation time. The dipole strength tensor is connected to the folded oscillator strength via

$$\mathbf{k}_\alpha^o\cdot\mathbf{S}(\omega)\mathbf{k}_\alpha^o = \sum_I f_{I\alpha}\tilde{g}(\omega - \omega_I), \qquad (40)$$

where $\tilde{g}(\omega)$ is the normalized Fourier transform of $g(t)$ and $\mathbf{k}_\alpha^o$ is the unit vector in the direction $\alpha = x, y, z$.

In addition to the linear regime, the time-propagation can be used to interrogate the nonlinear regime of the light-matter interaction. When an atom or a molecule resides in a laser field $\mathbf{E}(t) = \mathbf{E}_0\sin(\omega t)$ of frequency ω electrons begin to oscillate with this frequency. If the field is strong enough, nonlinear terms in the polarizability of the atom begin to contribute.[26] As a result, integer multiples of the field frequency, i.e., harmonics, appear in the emission spectrum. The intensities $\mathbf{H}$ of the emitted frequencies can be calculated from the acceleration of the dipole moment,[27] i.e.,

$$\mathbf{H}(\omega) \propto \left| \int_0^T dt \, \exp(i\omega t) \frac{d^2}{dt^2} g(t) [\boldsymbol{\mu}(t) - \boldsymbol{\mu}(0)] \right|^2. \quad (41)$$

In the present implementation of the time-propagation, the time-dependent equations are solved using the Crank–Nicolson propagator with a predictor-corrector step[28] (this choice is not unique, for other possible propagators see Ref. 29). The predictor-corrector scheme is required to efficiently handle the nonlinearity in the Hamiltonian, i.e., to obtain a reasonable approximation for the Hamiltonian in a future time. In the predictor step, the wave functions are propagated by approximating the Hamiltonian to be constant during the time step, i.e., $\widetilde{H}(t+\Delta t/2)=\widetilde{H}(t)+\mathcal{O}(\Delta t)$ and then solving a linear equation for the predicted future wave functions $\widetilde{\psi}_n^{\mathrm{pred}}(t+\Delta t)$,

$$(\widetilde{S} + i\widetilde{H}(t)\Delta t/2\hbar)\widetilde{\psi}_n^{\mathrm{pred}}(t+\Delta t)$$
$$= (\widetilde{S} - i\widetilde{H}(t)\Delta t/2\hbar)\widetilde{\psi}_n(t) + \mathcal{O}(\Delta t^2). \quad (42)$$

The Hamiltonian in the middle of the time step is approximated as

$$\widetilde{H}(t+\Delta t/2) = \tfrac{1}{2}(\widetilde{H}(t) + \widetilde{H}_{\mathrm{pred}}(t+\Delta t)), \quad (43)$$

where $\widetilde{H}_{\mathrm{pred}}(t+\Delta t)$ is obtained from the predicted wave functions. In the corrector step, the improved Hamiltonian $\widetilde{H}(t+\Delta t/2)$ is used to obtain the final, more accurate, propagated wave functions $\widetilde{\psi}_n(t+\Delta t)$ from

$$(\widetilde{S} + i\widetilde{H}(t+\Delta t/2)\Delta t/2\hbar)\widetilde{\psi}_n(t+\Delta t)$$
$$= (\widetilde{S} - i\widetilde{H}(t+\Delta t/2)\Delta t/2\hbar)\widetilde{\psi}_n(t) + \mathcal{O}(\Delta t^3). \quad (44)$$

The matrices in the linear equations [Eqs. (42) and (44)] are complex symmetric (not Hermitian), and we solve the equations using the biconjugate gradient stabilized method.[30]

As the Crank–Nicolson propagator is valid only for a short time step, repeated application of the propagator is required in any practical simulation. Note that no further improvement in the order of the error is obtained by repeating the corrector step with an improved approximation because the Crank–Nicolson itself is only accurate to the second order. Thus, in order to obtain more accurate results, it is more efficient to reduce the time step instead of repeating the correcting step more than once.

III. RESULTS AND DISCUSSION

In this section we will present example calculations for the linear-response and time-propagation schemes. The two computationally very different approaches are applied to the same systems and very good agreement is found in the linear-response regime. The strengths and weaknesses of both methods are discussed.

We apply consistently the LDA (Ref. 31) in all calculations. Zero Dirichlet boundary conditions are used for the finite systems studied both in the ground state as well as in the time-propagation calculations. A grid spacing of h =0.2 Å is used for the representation of the smooth wave functions unless otherwise specified.
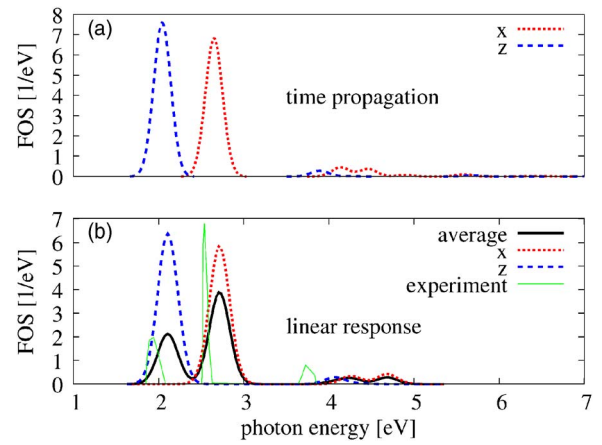

FIG. 1. (Color online) Optical absorption spectra of the Na_2 dimer represented as folded oscillator strengths [FOS's, Eq. (40)]. The results obtained (a) by the time-propagation after a delta kick and (b) by the linear-response scheme are compared. x and z denote the polarization directions of the light so that the molecule symmetry axis is aligned along the z direction. Experimental data is from Refs. 33 and 34 as quoted in Ref. 16.

Figure 1 shows a direct comparison of the absorption spectra of the Na_2 molecule at the experimental equilibrium distance of $R=3.068$ Å (Ref. 32) obtained via time-propagation after a delta kick and in the linear-response scheme. Both calculations are done using the simulation box of size $15 \times 15 \times 18$ Å^3. In the time-propagation calculation a perturbation strength of $\epsilon=1 \times 10^{-4}$, a grid spacing of h =0.3 Å, and a simulation time of 36 fs with a 1.2 as time step is used. The linear-response energy peaks are folded with Gaussians of width $\sigma=0.12$ eV corresponding to the Gaussian damping of the time-propagation. The simulated spectra agree perfectly. This proofs the correctness of the implementations of the two methods, which are technically very different. The shift of the peaks with respect to the experiment,[33,34] also seen in other calculations,[14,16,35] is probably related to the LDA.

In the next example we compare the absorption spectra of the benzene molecule obtained by the two methods. This molecule is one of the standard examples used in the literature.[14,17,36,37] The experimental spectrum shown in Fig. 2(c) consists of a strong peak at 6.9 eV and a broad feature in the range from 10 to above 25 eV. In Ref. 36 this experimental spectrum was nicely reproduced via a time-propagation scheme using a real-space grid, but in the linear-response calculation in Ref. 37 the energy of the first peak differed from the experimental value by ∼0.5 eV. In our calculations the linear-response and time-propagation results are in good agreement. The time-propagation calculation results in $f_I=1.2$ for the main peak at 6.74 eV and the linear-response calculation shows $f_I=1.3$ for the main peak at 6.85 eV. The positions and strengths of the main peak coincide well with the experimental values of 6.9 eV and $f=0.9$, respectively.[36]

The differences between the spectra of the linear-response and the time-propagation schemes seen in Fig. 2 originate from the different convergence behavior (see also Sec. IV below). The time-propagation uses only occupied states, but a large unit cell has to be used in order to avoid
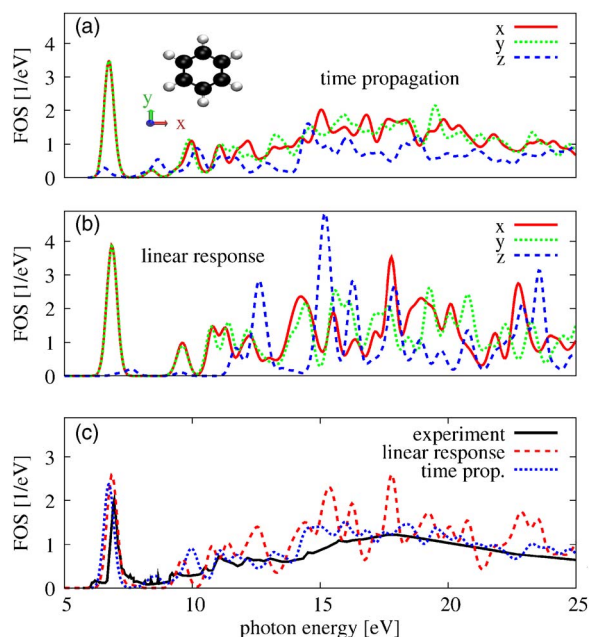
FIG. 2. (Color online) Optical absorption spectra of the benzene molecule represented as folded oscillator strengths [FOS's, Eq. (40)]. The results obtained (a) by the time-propagation after a delta kick and (b) by the linear-response scheme are shown. x, y, and z denote the polarization directions of the light as shown in the inset so that the z axis is perpendicular to the plane of the molecule. (c) The average spectra are compared with the experimental one quoted in Ref. 36. The experimental spectrum is scaled to integrate to $f=0.9$ in the energy range from 6.5 to 8.3 eV (Ref. 36).

spurious contributions from the simulation box boundaries. In contrast, the linear-response calculation has to sample unoccupied states in a range which is larger than the largest transition energy one is interested in. These unoccupied states belong already to the continuum of KS states. In practice a finite set of states can be sufficient to describe the essential features. This set is smaller if a smaller simulation box is chosen. We carry out the time-propagation with a box size of $18 \times 18 \times 13$ Å^3 and a simulation time of 24 fs with a time step of 1.2 arc sec. The linear-response calculation uses the finite box of $11 \times 11 \times 6$ Å^3 and the spectrum is folded with Gaussians of width $\sigma=0.2$ eV. Both calculations used a grid spacing of $h=0.25$ Å in this case.

A. Linear response

In the following we present results of linear-response calculations for selected divalent atoms and for Born–

Oppenheimer excited state potential surfaces of the Na dimer. These systems represent standard benchmarks. We will make use of the advantage that in the linear-response calculations both singlet and triplet (s/t) excitations are directly accessible.

Table I gives the lowest $S \rightarrow P$ s/t transition energies for selected divalent atoms. The present LDA results are compared to those obtained by pseudopotential calculations and to experimental values quoted in Ref. 16. In our calculations the real-space grid spans around the atom a cubic volume with the edge length of 12 Å. Our calculated excitation energies are in reasonable agreement with experiment and conform with the pseudopotential calculations with the exception of Zn and Cd. For these atoms differences up to 0.4 eV appear. They may be related to differences in the highest occupied orbital energies ϵ_{HOMO}^{LDA} also listed in Table I. We note that our ϵ_{HOMO}^{LDA} values obtained with the PAW method for Zn and Cd are in perfect agreement with the very accurate results of Ref. 38.

Next we turn our attention to the excited states of the Na$_2$ dimer. Usually, only the dipole spectrum at the equilibrium distance is studied.[14,16] We want to go further and investigate the Born–Oppenheimer potential surfaces as functions of the atomic separation R. Figure 3 shows the potentials of the ground state (X) and the lowest excited singlet (A,B) and triplet (x,a,b) states according to our calculations. These are performed using a rectangular calculation volume with the edge length of 8 Å perpendicular to and of $R+8$ Å parallel to the molecules axis. The energy axis is normalized to the LDA dissociation energy of the sodium dimer, i.e., twice the energy of a spin polarized Na atom. Note that the spin-compensated LDA ground-state energy does not converge toward this limit due to the self-interaction error.[39] Therefore the ground-state potential is above zero already at $R=6$ Å and the LDA triplet potential lowers below the ground-state potential for $R>4.2$ Å. The latter effect is called the triplet instability and it results in imaginary excitation energies. For this reason the lowest triplet state does not have a minimum in contrast to all other potentials shown. The properties of the potentials are further investigated in Table II in comparison to experimental data and configuration-interaction (CI) calculations from Refs. 40–42. Our equilibrium distances R_e and the vibrational frequencies ω_e are obtained by fitting the Morse potential to the potentials in Fig. 3. The range of 2 Å $\leq R \leq$ 4.8 Å is used to

TABLE I. Highest occupied KS orbital energies ϵ_{HOMO}^{LDA} and the lowest $S \rightarrow P$ s/t (spin singlet/triplet) excitation energies for selected divalent atoms. The present ground-state or linear-response LDA results (GPAW) are compared to similar literature results. Experimental excitation values taken from Ref. 16 are also given. All values are in eV.

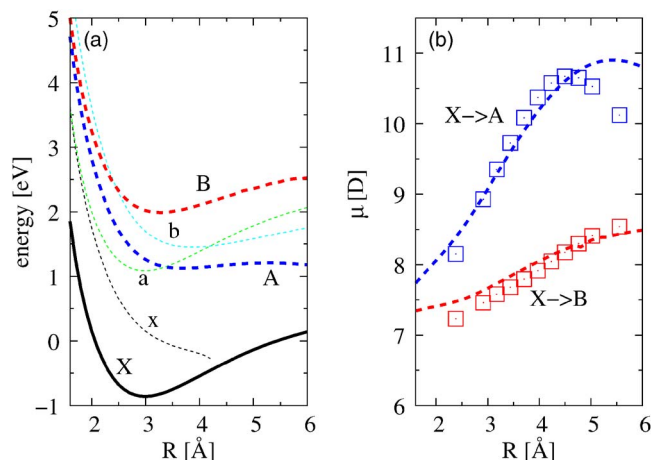|	ϵ_{HOMO}^{LDA} (eV)			$S \rightarrow P$ s/t		
Atom	Ref. 38	Ref. 16	GPAW	Ref. 16	GPAW	Expt.
Be	−5.60	−5.61	−5.60	4.94/2.45	4.82/2.41	5.28/2.72
Mg	−4.78	−4.78	−4.78	4.34/2.79	4.28/2.79	4.34/2.72
Ca	−3.86	−3.85	−3.85	3.22/1.93	3.18/1.97	2.94/1.89
Sr	−3.64	−3.59	−3.62	2.96/1.82	2.90/1.84	2.69/1.82
Zn	−6.21	−6.07	−6.21	5.71/4.27	5.89/4.41	5.79/4.05
Cd	−5.94	−5.56	−5.95	5.10/3.69	5.52/4.13	5.41/3.88

FIG. 3. (Color online) (a) Born–Oppenheimer potential curves for the Na$_2$ dimer in the ground state (X), in the lowest excited singlet states (A, B) and in the triplet states (x,a,b). (b) Comparison of the dipole transition moments calculated within the LDA (broken lines) with the CI results (squares) of Ref. 43. The dipole moment $\mu=|\boldsymbol{\mu}|$ is given in debyes (1 D=3.335 64 $\times 10^{-30}$ C m).

fit the X, a, b, and B potentials. The range has to be extended to 2 Å $\leq R \leq$ 8 Å for the A state due to the shallow potential minimum. The agreement of our excited state calculations with both experiment and CI approaches is reasonable and of similar quality as that for the ground-state calculation.

Our dipole transition moments [Eq. (23)] for the dipole allowed transitions $X \rightarrow A$ and $X \rightarrow B$ are compared in Fig. 3 with the results of the pioneering CI calculations by Stevens *et al.*[43] Our transition dipole moments calculated within the LDA are in a very good agreement with the CI results proving the accuracy of the linear-response TDDFT also for this quantity.

B. Time-propagation

Next, we present results of our time-propagation calculations in the nonlinear regime.

Figure 4 shows the calculated emission spectra of a Be atom exposed to laser fields of the frequency of 0.5 eV and strengths of E_0=0.2, 0.4, and 0.8 V/Å. Figure 5 shows similar results for the laser fields of the frequency of 1.0 eV. Only the odd harmonics are observed in the spectra as the

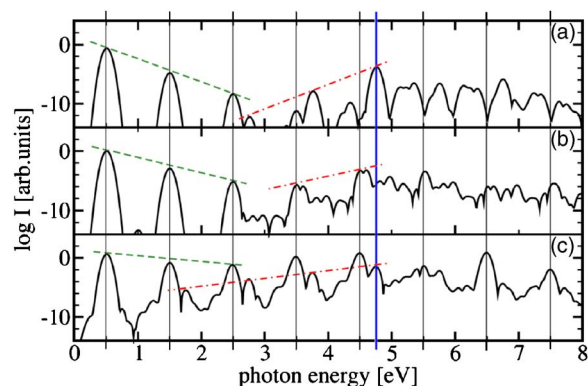FIG. 4. (Color online) Emission spectra of a Be atom in a sinusoidal dipole field of the frequency of 0.5 eV/$\hbar$ and strengths of (a) 0.2 V/Å, (b) 0.4 V/Å, and (c) 0.8 V/Å. The thick blue vertical line at 4.82 eV denotes the frequency of the first $S \rightarrow P$ transition. The thin vertical lines denote odd harmonic frequencies. The green dashed lines are drawn to emphasize the exponential decay of the high-harmonic peak intensities as a function of frequency in emission. The red dot-dashed lines emphasize the difference frequency mixing of the first resonance and the dipole field.

even harmonics are forbidden due to the spherical symmetry of the atom.[44] According to Figs. 4 and 5, the effect of a nearby resonance transition[45] is clearly apparent. The high-harmonic peaks near the first dipole allowed $^1S^e \rightarrow {}^3P^o$ transition at 4.82 eV gain intensity instead of decaying exponentially as function of the frequency. We observe in Fig. 4 the difference frequency mixing[44,45] of the first resonance and the sinusoidal field, i.e., a frequency equal to the difference of the first resonance and field frequencies appears. Note that we find perfect agreement in the energy of the first dipole allowed transition in the Be atom with the result of the linear-response calculation given in Table I. Comparing the oscillator strength of this transition we find f_I=1.35 consistently in both methods and in very good agreement with the result f_I=1.375 obtained by CI calculations in Ref. 46.

IV. CONVERGENCE PROPERTIES

A. Linear response

We will now discuss the convergence properties of the linear-response calculations. Figure 6(a) shows the relative deviation of the lowest excitation energies of the Be atom for different choices of the finite-difference parameter ε in the

TABLE II. Properties of the Born–Oppenheimer potentials for the Na$_2$ dimer. The transition energies T_e at the experimental equilibrium distance of R =3.068 Å are given in eV, the equilibrium distances R_e in Å, and the vibration energies ω_e in cm^{-1}. The experimental data is from Ref. 32 and the theoretical data from Refs. 40–42.

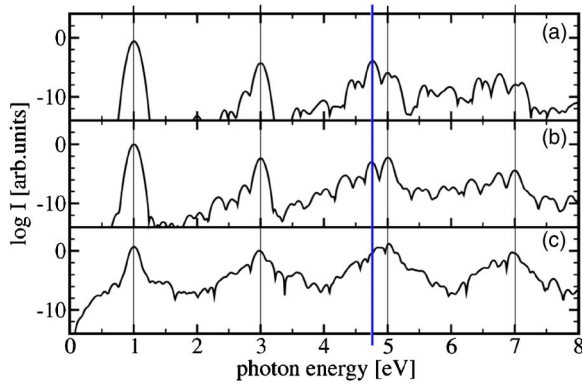| State	Present work			Expt.			CI calculations		
	T_e	R_e	ω_e	T_e	R_e		T_e	R_e[a]	ω_e[a]
$X\ ^1\Sigma_g^+$		2.99	161		3.07	159		3.17	145
$x\ ^2\Sigma_u^+$	0.96	⋯	⋯	⋯	⋯	⋯	1.05[a]/0.99[b]	5.20	29
$a\ ^3\Pi_u^+$	1.86	2.98	155	⋯	⋯	⋯	1.60[a]/1.56[b]	3.21	146
$A\ ^1\Sigma_u^+$	2.13	3.75	85	1.82	3.64	117	1.86[a]/1.82[b]	3.75	115
$b\ ^3\Sigma_g^+$	2.37	3.87	97	⋯	⋯	⋯	2.34[a]/2.26[c]	3.91	101
$B\ ^3\Sigma_g^+$	2.41	3.42	126	2.52	3.42	124	2.62[a]/2.52[c]	3.63	106

[a]Reference 40.
[b]Reference 41.
[c]Reference 42.

FIG. 5. (Color online) Emission spectra of a Be atom in a sinusoidal dipole field of the frequency of 1.0 eV/$\hbar$ and strengths of (a) 0.2 V/Å, (b) 0.4 V/Å, and (c) 0.8 V/Å.

calculation of the XC kernel according to Eq. (20). Too large values of ε lead out of the perturbation regime, whereas too small values of ε produce numerical errors. However, the figure shows that the results are quite insensitive to the choice of the parameter, i.e., it can be chosen in the range of $10^{-12} < \varepsilon < 0.01$ resulting in the uncertainty of less than 0.1% in the excitation energy. The effect of the size of the KS excitation basis is much more severe as shown in Fig. 6(b) for the same excited states. Here the number j of unoccupied states is varied. The three lowest unoccupied KS orbitals have the symmetry corresponding to the angular momentum $l = 1$. Restricting the calculation to these states can describe only the excitations $^1S \rightarrow ^{1/3}P^o$. Including the next $l = 0$ orbital ($j > 3$) enables the appearance of the $^1S \rightarrow ^3S$ transition, but does not change the energies of the $^{1/3}P^o$ excited states. Incorporating more unoccupied orbitals of the $l = 1$ symmetry
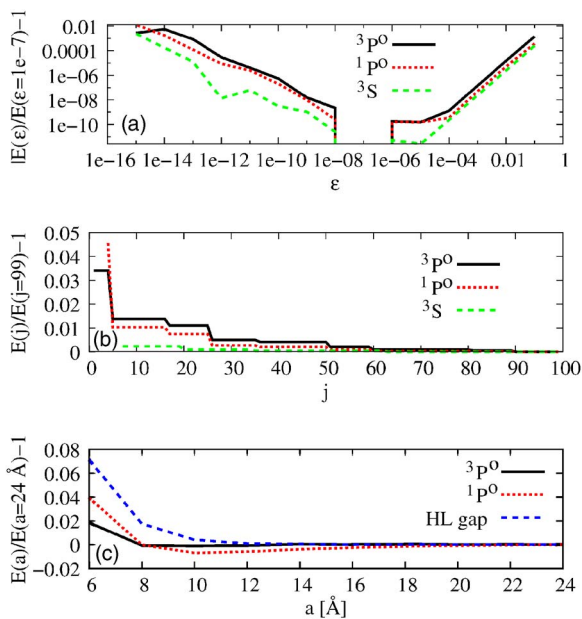

FIG. 6. (Color online) Convergence of the HOMO-LUMO gap and the excitations to the lowest ^3S, $^1P^o$, and $^3P^o$ states calculated in the linear-response scheme for the Be atom. The convergence is given as a function of (a) the finite-difference parameter ε for evaluation of the xc kernel [Eq. (20)], (b) the number j of unoccupied orbitals taken into account in the calculation, and (c) dependence on the edge length a of the cubic simulation box.
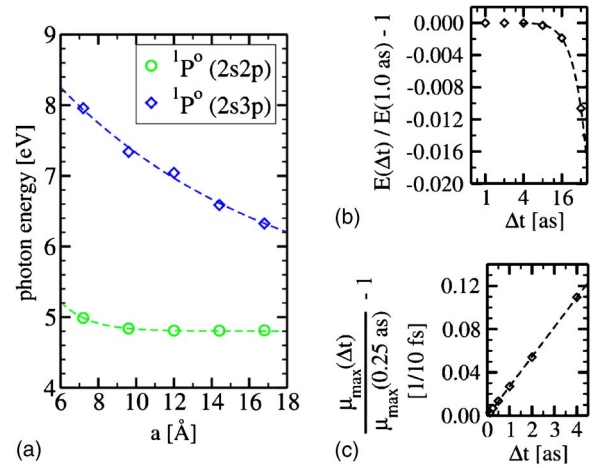

FIG. 7. (Color online) (a) Convergence of the linear-response transition energies of the Be atom as a function of the edge length a of the cubic simulation box. The dashed lines are exponential fits. (b) Convergence of the energy of the first transition as a function of the length Δt of the time step. The dashed line is a quadratic fit. (c) Convergence of the peak dipole moment as a function of the length Δt of the time step. The dashed lines is a linear fit.

produces changes of the energy of the $^{1/3}P^o$ excited state due to coupling to the $2s \rightarrow 2p$ KS transitions seen as steps in Fig. 6(b). The ^3S excited state energy is not affected due to the different symmetry of the KS transitions. Note that we have used 100 KS states to calculate the excitations of the Be atom. Such a large number of unoccupied states is not practical, but Fig. 6(b) shows also that an accuracy of more than 2% is reached already by the inclusion of a few unoccupied orbitals. Finally, we have studied the convergence as a function of the box size used for the real-space grids. The results are shown in Fig. 6(c). We use a cubic box with the edge length a, and vary a from 6 to 24 Å in steps of 2 Å. The highest occupied to lowest unoccupied orbital (HOMO-LUMO) gap shows convergence at $a \approx 10$ Å. The triplet ($^3P^o$) energy converges for even smaller box sizes, obviously due to a cancellation of errors. The slowest convergence is found for the singlet state ($^3P^o$) due to effect of the long-range RPA kernel not contributing to the triplet-state energy. However, the effect is well below 0.1 eV and therefore much lower than the accuracy of the TDDFT found above and in other calculations.[13]

B. Time-propagation

The convergence of the time-propagation method depends mainly on two factors: the simulation box size and the length of the time step. The box size should be considerably larger than that required for the ground-state calculation as excited states are more diffuse. The convergence of the first and the second transition energies of the Be atom are shown Fig. 7(a) as a function of the length a of the cubic simulation box. The second transition energy converges clearly slower than that of the first one. The latter has converged already around $a = 5$ Å. Figure 7(b) shows the convergence of the first transition energy as a function of the length of the time step Δt. The transition energy behaves quadratically and it has converged around $\Delta t = 8$ as, whereas the corresponding
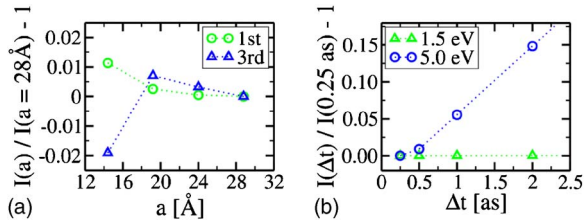
FIG. 8. (Color online) (a) Convergence of the harmonic peak intensities as a function of the edge length a of the cubic simulation box. The dotted lines are just a guide to the eye. (b) Convergence of the harmonic peak intensities as a function of the length Δt of the time step. The dotted lines are just a guide to the eye.

peak intensity in Fig. 7(c) converges only linearly in this range and time steps down to $\Delta t = 1-2$ as must be used in order to obtain accurate results. The f-sum rule (or Thomas–Reiche–Kuhn sum rule),[47] $\int S_{ij}(\omega)d\omega = N\delta_{ij}$, where N is the number of electrons, is fulfilled within a few percent in the present calculations. Note that care must be taken when constructing the PAW-projectors, because, if pseudo-wavefunctions represented in the grid cannot be accurately transformed to the atomic basis by the PAW-projectors, the f-sum becomes incomplete.

Figure 8(a) shows the convergence of the intensities of the first and third harmonics as function of the edge length a of the cubic simulation box. The difference ΔI is taken with respect to the value at $a=28$ Å. Naturally, higher harmonics require a larger simulation box. For the harmonics near and beyond the first transition resonance we are not able to find converged results within our computer resources. The reason is that a part of the system is excited to the first excited state, from which it is more easily ionized by the laser field than from the ground state.

Figure 8(b) shows the convergence of the peak intensities at 1.5 and 5.0 eV as a function of the length of the time step Δt. The difference ΔI is taken with respect to the value at $\Delta t=0.25$ as. The third harmonic intensity at 1.5 eV is almost independent on Δt, whereas near (and beyond) the first transition resonance at 5.0 eV the intensity difference depends linearly on Δt.

V. CONCLUSION

We have described the implementation of the time-dependent density-functional theory in the projector augmented-wave framework, both in the time-propagation as well as within the linear-response scheme. The two approaches were compared by calculating the optical absorption spectra of Na_2 and C_6H_6 molecules in the linear regime. Good agreement of the absorption spectra was found, proving the correctness of both implementations. The strengths and weaknesses of both methods were discussed and examples of the possibilities were given. For example, the ability of the time-propagation scheme to describe nonlinear effects was demonstrated in the case of the Be atom. The convergence properties of both methods were studied in detail.

APPENDIX A: AUGMENTATION SPHERE CORRECTIONS (THE RPA PART)

This Appendix gives the explicit forms of the augmentation-sphere corrections.

Due to the use of compensation charges, all terms appearing in the augmentation-sphere corrections to the RPA part are local and can be expressed by integrals of the following type:

$$(f|g)_a := \int_a \int_a d\mathbf{r}_1 d\mathbf{r}_2 \frac{f^*(\mathbf{r}_1)g(\mathbf{r}_2)}{|\mathbf{r}_1 - \mathbf{r}_2|}, \tag{A1}$$

where we have used the shorthand a for the restriction $|\mathbf{r}_{1/2} - \mathbf{R}_a| < r_c^a$. Here, r_c^a is the radius of the augmentation sphere for the atom at $\mathbf{R}_a$. Using Eq. (13) the correction $\Delta K_{ij,kq}^{RPA,a}$ can be written as

$$\Delta K_{ij,kq}^{RPA,a} = (n_{ij}^a|n_{kq}^a)_a - (\widetilde{n}_{ij}^a + \widetilde{Z}_{ij}^a|\widetilde{n}_{kq}^a + \widetilde{Z}_{kq}^a)_a. \tag{A2}$$

Inserting the explicit forms of pair densities and compensation charges leads to the expression

$$\Delta K_{ij,kq}^{RPA,a} = 2 \sum_{i_1 i_2 i_3 i_4} P_{ii_1}^a P_{ji_2}^a P_{ki_3}^a P_{qi_4}^a C_{i_1 i_2 i_3 i_4}^a, \tag{A3}$$

with the coefficients $C_{i_1 i_2 i_3 i_4}^a$ given in Eq. (C3) of Ref. 19. These coefficients have to be calculated only once for each type of atom.

APPENDIX B: AUGMENTATION SPHERE CORRECTIONS (THE xc KERNEL)

The local corrections to the exchange-correlation kernel in the finite-difference scheme can be written as

$$\Delta K_{ij\sigma,kq\tau}^{xc,a} = \lim_{\varepsilon \to 0} \frac{K_{ij\sigma,kq}^{xc,a,+} - K_{ij\sigma,kq}^{xc,a,-}}{2\varepsilon}, \tag{B1}$$

with

$$K_{ij\sigma,kq\tau}^{xc,a,\pm} = \langle \psi_{i\sigma}^a | v_{xc}[n_\sigma^a, n_\tau^a \pm \varepsilon n_{kq\tau}^a] | \psi_{j\tau}^a \rangle$$
$$- \langle \widetilde{\psi}_{i\sigma}^a | v_{xc}[\widetilde{n}_\sigma^a, \widetilde{n}_\tau^a \pm \varepsilon \widetilde{n}_{kq\tau}^a] | \widetilde{\psi}_{j\sigma}^a \rangle. \tag{B2}$$

Using the expansion of the wave functions in Eq. (3) we obtain

$$K_{ij\sigma,kq\tau}^{xc,a,\pm} = \sum_{i_1 i_2} P_{i\sigma i_1} P_{j\sigma i_2} I_{i_1 i_2}^{a,kq\tau,\pm}. \tag{B3}$$

Above, we have defined the integral

$$I_{i_1 i_2}^{a,kq\tau,\pm} = \int_a d\mathbf{r} [\phi_{i_1}(\mathbf{r}) \phi_{i_2}(\mathbf{r}) v_{xc}[n_\sigma, n_{kq\tau}^{\pm}]$$

$$- \tilde{\phi}_{i_1}(\mathbf{r}) \tilde{\phi}_{i_2}(\mathbf{r}) v_{xc}[\tilde{n}_\sigma, \tilde{n}_{kq\tau}^{\pm}]], \tag{B4}$$

with the shorthands $n_{kq}^{\pm} = n_\tau^a \pm \varepsilon n_{kq\tau}^a$ and $\tilde{n}_{kq}^{\pm} = \tilde{n}_\tau^a \pm \varepsilon \tilde{n}_{kq\tau}^a$. Above, v_{xc} depends on the modified atomic density matrix compared to the $D_{i_1 i_2}^a$ in Eq. (7). A density change by $\pm \varepsilon n_{kq\tau}$ results in a change in $D_{i_1 i_2}^a$ as

$$n^a(x) \pm \varepsilon n_{kq}^a(x) = \sum \bar{D}_{i_1 i_2, kq}^{a,\pm} \phi_{i_1}^a(x) \phi_{i_2}^a(x), \tag{B5}$$

with

$$\bar{D}_{i_1 i_2, kq}^{a,\pm} = D_{i_1 i_2}^a \pm \frac{\varepsilon}{2} (P_{k i_1} P_{q i_2} + P_{k i_2} P_{q i_1}), \tag{B6}$$

where we have used a symmetric notation to point out the exchange symmetry with respect to $i_1 \leftrightarrow i_2$. The integrals [Eq. (B4)] are evaluated numerically as described in Ref. 19.

[1] W. Kohn and L. J. Sham, Phys. Rev. **140**, A1133 (1965).
[2] P. Hohenberg and W. Kohn, Phys. Rev. **136**, B864 (1964).
[3] E. Runge and E. K. U. Gross, Phys. Rev. Lett. **52**, 997 (1984).
[4] M. E. Casida, in *Recent Developments and Applications in Modern Density-Functional Theory*, edited by J. M. Seminario (Elsevier, Amsterdam, 1996), p. 391.
[5] K. Yabana and G. F. Bertsch, Phys. Rev. B **54**, 4484 (1996).
[6] G. Senatore and K. R. Subbaswamy, Phys. Rev. A **35**, 2440 (1987).
[7] S. J. van Gisbergen, J. G. Snijders, and E. J. Baerends, Phys. Rev. Lett. **78**, 3097 (1997).
[8] J.-I. Iwata, K. Yabana, and G. F. Bertsch, J. Chem. Phys. **115**, 8773 (2001), and references therein.
[9] G. Onida, L. Reining, and A. Rubio, Rev. Mod. Phys. **74**, 601 (2002).
[10] R. Bauernschmitt and R. Ahlrichs, Chem. Phys. Lett. **256**, 454 (1996).
[11] A. Tsolakidis, D. Sánchez-Portal, and R. M. Martin, Phys. Rev. B **66**, 235416 (2002).
[12] N. L. Doltsinis and M. Sprik, Chem. Phys. Lett. **330**, 563 (2000).
[13] M. Moseler, H. Häkkinen, and U. Landman, Phys. Rev. Lett. **87**, 053401 (2001).
[14] X. Qian, J. Li, X. Lin, and S. Yip, Phys. Rev. B **73**, 035408 (2006).
[15] B. Walker and R. Gebauer, J. Chem. Phys. **127**, 164106 (2007).
[16] I. Vasiliev, S. Ögüt, and J. R. Chelikowsky, Phys. Rev. Lett. **82**, 1919 (1999).
[17] M. A. L. Marques, A. Castro, G. F. Bertsch, and A. Rubio, Comput. Phys. Commun. **151**, 60 (2003).
[18] P. E. Blöchl, Phys. Rev. B **50**, 17953 (1994).
[19] J. J. Mortensen, L. B. Hansen, and K. W. Jacobsen, Phys. Rev. B **71**, 035109 (2005).
[20] See https://wiki.fysik.dtu.dk/gpaw.
[21] M. Casida, in *Recent Advances in Density Functional Methods, Part I*, edited by D. Chong (World Scientific, Singapore, 1995), p. 155.
[22] F. Furche, J. Chem. Phys. **114**, 5982 (2001).
[23] A. Putrino, D. Sebastiani, and M. Parrinello, J. Chem. Phys. **113**, 7102 (2000).
[24] D. Egli and S. R. Billeter, Phys. Rev. B **69**, 115106 (2004).
[25] M. Mundt and S. Kümmel, Phys. Rev. B **76**, 035413 (2007).
[26] T. Brabec and F. Krausz, Rev. Mod. Phys. **72**, 545 (2000).
[27] M. Protopapas, C. H. Keitel, and P. L. Knight, Rep. Prog. Phys. **60**, 389 (1997).
[28] W. H. Press, B. P. Flannery, S. A. Teukolsky, and W. T. Vetterling, *Numerical Recipes in C* (Cambridge University Press, Cambridge, 1992).
[29] A. Castro, M. A. L. Marques, and A. Rubio, J. Chem. Phys. **121**, 3425 (2004).
[30] R. Barrett, M. Berry, T. F. Chan, J. Demmel, J. Donato, J. Dongarra, V. Eijkhout, R. Pozo, C. Romine, and H. V. der Vorst, *Templates for the Solution of Linear Systems: Building Blocks for Iterative Methods*, 2nd ed. (SIAM, Philadelphia, PA, 1994).
[31] J. P. Perdew and Y. Wang, Phys. Rev. B **46**, 12947 (1992).
[32] K. Huber and G. Herzberg, *Constants of Diatomic Molecules*, NIST Chemistry WebBook, NIST Standard Reference Database Number 69, edited by P. J. Linstrom and W. G. Mallard (National Institute of Standards and Technology, Gaithersburg MDY, 2003). See http://webbook.nist.gov; data prepared by J. W. Gallagher and R. D. Johnson III.
[33] W. R. Fredrickson and W. W. Watson, Phys. Rev. **30**, 429 (1927).
[34] S. P. Sinha, Proc. Phys. Soc., London, Sect. A **62**, 124 (1949).
[35] M. A. L. Marques, A. Castro, and A. Rubio, J. Chem. Phys. **115**, 3006 (2001).
[36] K. Yabana and G. F. Bertsch, Int. J. Quantum Chem. **75**, 55 (1999).
[37] I. Vasiliev, S. Ogut, and J. R. Chelikowsky, Phys. Rev. B **65**, 115416 (2002).
[38] S. Kotochigova, Z. Levine, E. Shirley, M. Stiles, and C. Clark, *Atomic Reference Data for Electronic Structure Calculations* (National Institute of Standards and Technology, Gaithersburg, MD, 2004). Online available: http://physics.nist.gov/PhysRefData/DFTdata/contents.html.
[39] E. J. Baerends, Phys. Rev. Lett. **87**, 133004 (2001).
[40] D. D. Konowalow, M. E. Rosenkrantz, and M. L. Olson, J. Chem. Phys. **72**, 2612 (1980).
[41] V. Bonacic-Koutecky, P. Fantucci, and J. Koutecký, J. Chem. Phys. **93**, 3802 (1990).
[42] H.-K. Chung, K. Kirby, and J. F. Babb, Phys. Rev. A **63**, 032516 (2001).
[43] W. J. Stevens, M. M. Hessel, P. J. Bertoncini, and A. C. Wahl, J. Chem. Phys. **66**, 1477 (1977).
[44] T. Brabec and F. Krausz, Phys. Rev. **127**, 1918 (1962).
[45] R. W. Boyd, *Nonlinear Optics*, 2nd ed. (Academic, New York, 2003).
[46] J. Fleming, M. R. Godefroid, K. L. Bell, A. Hibbert, N. Vaeck, J. Olsen, P. Jonsson, and C. F. Fischer, J. Phys. B **29**, 4347 (1996).
[47] S. Wang, Phys. Rev. A **60**, 262 (1999).